

Spectral relaxation computation of Maxwell fluid flow from a stretching surface with quadratic convection and non-Fourier heat flux using Lie symmetry transformations**M. M. Bhatti^{1,*}, A. Shahid², Ioannis E. Sarris³ and O. Anwar Bég⁴**¹College of Mathematics and Systems Science, Shandong University of Science and Technology, Qingdao 266590, Shandong, **China**²School of Science, Zhejiang University of Science and Technology, Hangzhou, 310023, P.R. **China**³Department of Mechanical Engineering, University of West Attica, 12244 Athens, **Greece**⁴Professor and Director-Multi-Physical Engineering Sciences Group, Mechanical Engineering Department, School of Science, Engineering and Environment (SEE), University of Salford, Manchester, **UK***Correspondence: mmbhatti@sdust.edu.cn

Abstract: A mathematical model for nonlinear quadratic convection with non-Fourier heat flux in coating boundary layer flow of a Maxwell viscoelastic fluid is presented. Nonlinear quadratic thermal radiation and heat source/sink effects are also considered. The transformations of Lie symmetry are employed. The resultant nonlinear differential equations with defined boundary conditions are numerically solved using the spectral relaxation technique (SRM), a robust computational methodology. Graphical visualization of the velocity and temperature profiles is included for a range of different emerging parameters. For skin friction and the Nusselt number, numerical data is also provided. There is a very strong correlation between the outcomes of the current study and those published in the literature. Higher values of the nonlinear thermal radiation, mixed convection, thermal conductivity, nonlinear convection, and heat source/generation parameters increase temperature as well as the thickness of the thermal boundary layer. However, a higher Prandtl number, thermal relaxation parameter, and heat sink/absorption parameter all reduce temperature. Deborah number causes velocity to be raised (and momentum boundary layer thickness to be lowered), whereas raising nonlinear mixed convection parameter causes velocity to be decreased (and momentum boundary layer thickness to be increased), and a velocity overshoot is calculated. The models are applicable to simulations of high-temperature polymeric coatings in material processing.

Keywords: *Maxwell fluid; nonlinear quadratic convection; non-Fourier heat flux; Lie symmetry transformation; computational spectral approach.*

1. Introduction

Mixed convection, which occurs when there are both forced and free convection flows present, has a wide range of applications. These include heat exchangers, solar thermal systems, electronic systems and drying systems. The temperature differences arising in various practical applications can be excessive; consequently, the density in the buoyancy term (upward force) varies in a nonlinear fashion in response to changes in temperature. The nonlinear density temperature fluctuation has an essential impact on the flow field. Thus, the presence of quadratic density variation with temperature is important for determining the heat transfer rate in the boundary layer flow. This is referred as *quadratic thermal convection*. Goren [1] introduced this nonlinear convection term in the following form: $\Delta\rho = -\rho\beta(T - T_{\text{amb}})^2$ with β represents the thermal expansion coefficient with second order. With the nonlinear Boussinesq approximation, he observed a significant change in the heat transfer characteristics. Later, using various Newtonian and non-Newtonian fluid models, multiple authors investigated nonlinear quadratic convection in various geometrical configurations. Mahanthesh *et al.* [2] addressed quadratic convection in dusty Casson and Carreau flow from a stretched surface, taking into account nonlinear thermal radiation, non-uniform heat source/sink, and convective wall condition effects. Hayat *et al.* [3] employed a non-Darcy model to examine nonlinear convection with heat and mass transport in porous media. Unsteady Casson nanofluid flow through a cylinder with quadratic convection was also explored by Reddy *et al.* [4]. Akolade [5] studied non-Newtonian squeezing flow with quadratic convection and velocity slip effects. Patil *et al.* [6] reported on quadratic convection in triple-diffusive nonlinear nanofluid convection flow external to a wedge. Shahid *et al.* [7] investigated bi-directional non-Newtonian convective flow along a stretched surface using a spectral technique.

Thermal radiation is associated with high temperature phenomena and arises in many applications in engineering and science, including nuclear reactor cooling, combustion processes, space technology, power generation and materials fabrication. In the past years many authors used nonlinear and linear thermal radiation flux models to study radiative effects in various flows of both Newtonian and non-Newtonian fluent media. For instance, Shaw *et al.* [8] computed the nonlinear thermal radiation effects in hybrid Cross non-Newtonian nanofluid and quadratic convection at different Prandtl numbers with a Runge-Kutta method. The consequences of Brownian motion and thermophoresis on bioconvection nanofluid mobility with nonlinear thermal radiation, magnetic field, and quadratic chemical process effects were thoroughly studied by Makinde and Animasaun [9]. Sreedevi *et al.* [10] compared the hybrid nanofluid flow transport characteristics across a wedge with Al_2O_3 and TiO_2 nanoparticles under nonlinear thermal radiation using a Galerkin finite element technique. The consequences of nonlinear thermal radiation and activation energy on viscoelastic second-grade convective flow were modelled by Khan *et al.* [11]. Khan *et al.* [12] explored the impact of thermal stratification and nonlinear thermal radiation on a Sutterby fluid's convective flow. The numerical solutions were analyzed using the bvp4c method. Mahanthesh *et al.* [13] computed the effects of nonlinear thermal radiation and quadratic convection on multiphase flow from a vertical plate with a finite difference technique. Unsteady boundary layer flow including quadratic convection, multiple diffusions, and nonlinear thermal radiation was the focus of an entropy research by Patil and Goudar [14]. In order to model convective flows of Oldroyd-B and Casson non-Newtonian fluids in the presence of nonlinear thermal radiation and chemical reactivity, Algehyne *et al.* [15] employed the homotopy approach. All these investigations showed a strong modification in thermal characteristics with radiative flux and quadratic convection effects.

The above studies were generally confined to the classical Fourier heat flux model [16] which neglects thermal relaxation effects and is parabolic in nature. Cattaneo [17] extended

Fourier's [16] theory by including thermal relaxation time effects producing a hyperbolic model. Later, Christov [18] expanded on the Cattaneo model [17] by including the Oldroyd upper convected derivative. Later, the generalised Cattaneo-Christov heat-flow model was used in several experiments. For instance, Bissell [19] used the Cattaneo-Christov heat-flow model to study thermal convection in a magnetized fluid. Layek and Pati [20] investigated the behavior of the Fourier heat flow model with convection, chaos, and bifurcation phenomena. Mehmood *et al.* [21] used the non-Fourier heat flux model to explore oblique stagnation point flow of an Oldroyd-B fluid, taking into account chemical reaction and magnetic field implications. Shamshuddin *et al.* [22] evaluated swirling thermal convection between co-axial spinning disks using a non-Fourier heat flow model and a perturbation approach. They discovered a suppression in Nusselt number at the bottom disk with larger non-Fourier (thermal relaxation parameter) values, which is due to the delay in thermal diffusion in the fluid. Gangadhar *et al.* [23] used a Cattaneo-Christov heat flow model with linear thermal radiation and a Keller-box finite difference technique to investigate the hydromagnetic Maxwell viscoelastic nanofluid convection flow. They studied both single-walled and multi-walled carbon nanotube-based nanofluids and discovered that thermal relaxation time and temperature are inversely related. Ibrahim *et al.* [24] used a Galerkin finite element approach to evaluate non-Fourier Oldroyd-B transport from a stretched surface in the presence of heat production and absorption. Khan *et al.* [25] investigated the effects of Cattaneo-Christov heat flux, nonlinear thermal radiation, and activation energy on the flow of a second grade viscoelastic nanofluid. Waqas *et al.* [26] used a non-Fourier heat flux model with activation energy effects to investigate the dynamics of third grade non-Newtonian bioconvection nanofluids. Turkyilmazoglu [27, 28] addressed the non-Fourier Cattaneo-Christov heat flux model and exponential wall heating with natural convection via a square cavity. Bejawada *et al.* [29] investigated the impact of radiation on chemical reactions through a nonlinear surface using a non-Darcy model. To investigate the flow's rheology, they used the magnetized casson fluid model. Thermal radiation with viscous dissipation and natural convection via a stretched surface was explored by Nalivela *et al.* [30]. Khan *et al.* [31] investigated the heat transfer radiation influence on micropolar fluids with varying thermal applications using solutal boundary conditions.

According to a review of the literature, the nonlinear quadratic convective boundary layer flow of a viscoelastic Maxwell fluid from a stretched surface with nonlinear quadratic convection and nonlinear quadratic heat radiation has not been studied. This is the present study's emphasis and uniqueness, which also incorporates heat source/sink and temperature-dependent thermal conductivity characteristics. Temperature is well known to cause significant changes in physical properties and thermal conductivity variation has been identified as an important aspect of modern polymer processing [32]. Radiative effects in non-Newtonian polymer coatings are also important in the development of emerging multilayer sol-gel optical high reflector surfacing [33]. It is important also to address radiative heat transfer in designing more robust thermal barrier coatings (e. g. LPCVD ZrB₂ coatings) for gas turbine blades using optically opaque materials under high convective flow conditions [34-38]. Motivated by these applications, a two-dimensional mathematical model is developed for steady non-Fourier non-Newtonian coating flow. A group of Lie transformations is deployed. The revised conservation boundary layer equations and accompanying boundary conditions are investigated numerically using the spectral relaxation technique. The spectral relaxation technique (SRM) solves nonlinear boundary value problems of multi-physical reactive magnetic rheological fluids on complicated surfaces with great accuracy and numerical stability. The graphical and numerical results for selected physical variables are presented, along with a comparison to previously published findings.

2. Mathematical model for Maxwell non-Fourier boundary layer coating flow

An incompressible boundary layer coating convection flow of a Maxwell viscoelastic fluid over a vertically stretchy stretching surface with non-linear thermal radiation and heat source/sink effects is considered. In order to study the impacts of relaxation on the heat transfer characteristics, non-Fourier (Cattaneo-Christov) heat flux is also taken into consideration. The x –axis and y –axis of a cartesian coordinate system are oriented along the elastic (stretchy) surface and the normal direction, respectively. The assumed surface temperature is T_s , whereas the anticipated ambient temperature is T_{amb} . Furthermore, $u_w = sx$, where s stands for the stretching rate, provides the surface's stretching (or elastic) velocity. In Fig. 1 below, the physical model is shown.

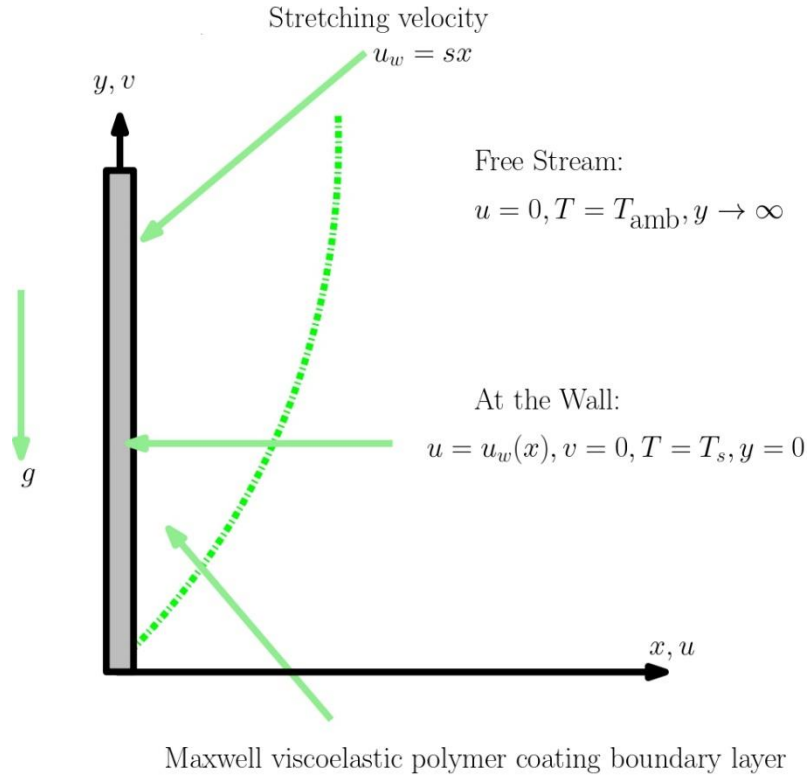


Fig. 1 Non-Fourier viscoelastic convective coating flow

Considering these assumptions, the conservation boundary layer equations, including the continuity, momentum, and energy equations, may be written as follows [39-40]:

$$\frac{\partial u}{\partial x} + \frac{\partial v}{\partial y} = 0, \quad (1)$$

$$\begin{aligned} u \frac{\partial u}{\partial x} + v \frac{\partial u}{\partial y} + M \left(u^2 \frac{\partial^2 u}{\partial x^2} + v^2 \frac{\partial^2 u}{\partial y^2} + 2uv \frac{\partial^2 u}{\partial x \partial y} \right) \\ = v \frac{\partial^2 u}{\partial y^2} + g[\beta(T - T_{amb}) + \beta_1(T - T_{amb})^2], \end{aligned} \quad (2)$$

$$\begin{aligned} u \frac{\partial T}{\partial x} + v \frac{\partial T}{\partial y} + N_f \left(u \frac{\partial u}{\partial x} \frac{\partial T}{\partial x} + v \frac{\partial v}{\partial y} \frac{\partial T}{\partial y} + v \frac{\partial u}{\partial y} \frac{\partial T}{\partial x} + u \frac{\partial v}{\partial x} \frac{\partial T}{\partial y} + 2uv \frac{\partial^2 T}{\partial y \partial x} + u^2 \frac{\partial^2 T}{\partial x^2} \right. \\ \left. + v^2 \frac{\partial^2 T}{\partial y^2} \right) = \frac{1}{\rho C_p} \frac{\partial}{\partial y} \left(\kappa(T) \frac{\partial T}{\partial y} \right) + \frac{Q}{\rho C_p} (T - T_{amb}) - \frac{\partial q}{\partial y}, \end{aligned} \quad (3)$$

Here M represents the rheological relaxation time, ν represents the kinematic viscosity, g represents the gravity, β, β_1 represent the linear and nonlinear thermal expansion coefficients, N_f represents the Cattaneo-Christov heat-flux relaxation time, ρ the density, C_p the specific heat, Q the heat generation/absorption coefficient, q the radiative heat flux, and $\kappa(T)$ represents the variable thermal conductivity.

It has been discovered that the thermal conductivity κ of liquid metals changes with temperature in an almost linear way in the region 0° to 400°F . (see Kays [41]). As in [42], we suppose that the thermal conductivity κ has the following form.

$$\kappa(T) = \kappa_{\text{amb}} \left(1 + \epsilon \frac{T - T_{\text{amb}}}{T_s - T_{\text{amb}}} \right), \quad (4)$$

The nonlinear radiative heat flux is defined as:

$$q = -\frac{4\sigma^*}{3k^*} \frac{\partial(T^4)}{\partial y}, \quad (5)$$

Where κ_{amb} represents the ambient thermal conductivity, ϵ represents the variable thermal conductivity parameter, σ^* the Stefan-Boltzmann constant, k^* represents the coefficient of mean absorption. An optically thick viscoelastic fluid is assumed, and the radiative flux is unidirectional. The temperature in equation (5) may be examined in terms of ambient temperature using the Taylor series expansion procedure, as shown below [43-44]:

$$T^4 = T_{\text{amb}}^4 + 4(T - T_{\text{amb}})T_{\text{amb}}^3 + 6(T - T_{\text{amb}})^2T_{\text{amb}}^2 + \dots, \quad (6)$$

The higher terms can be ignored after the quadratic terms in the above equation, giving:

$$T^4 = 4T_{\text{amb}}^4 - 8TT_{\text{amb}}^3 + 6T^2T_{\text{amb}}^2. \quad (7)$$

The following are the specified boundary conditions for both the free stream and the surface:

$$u = u_w(x), v = 0, T = T_s \quad \text{at} \quad y = 0. \quad (8)$$

$$u \rightarrow 0, T \rightarrow T_{\text{amb}} \quad \text{as} \quad y \rightarrow \infty. \quad (9)$$

Considering the non-dimensional quantities listed below:

$$\tilde{x} = \frac{xs}{u_w}, \tilde{y} = y\sqrt{\frac{s}{\nu}}, \tilde{u} = \frac{u}{u_w}, \tilde{v} = (\nu s)^{-1/2}v, T = T_{\text{amb}}[1 + \tilde{T}(\tilde{T}_s - 1)], \tilde{T}_s = \frac{T_s}{T_{\text{amb}}}. \quad (10)$$

Invoking Eqn. (10) in Eqns. (1)-(3), we get:

$$\frac{\partial \tilde{u}}{\partial \tilde{x}} + \frac{\partial \tilde{v}}{\partial \tilde{y}} = 0, \quad (11)$$

$$\tilde{u} \frac{\partial \tilde{u}}{\partial \tilde{x}} + \tilde{v} \frac{\partial \tilde{u}}{\partial \tilde{y}} + \alpha \left(\tilde{u}^2 \frac{\partial^2 \tilde{u}}{\partial \tilde{x}^2} + \tilde{v}^2 \frac{\partial^2 \tilde{u}}{\partial \tilde{y}^2} + 2\tilde{u}\tilde{v} \frac{\partial^2 \tilde{u}}{\partial \tilde{x}\partial \tilde{y}} \right) = \frac{\partial^2 \tilde{u}}{\partial \tilde{y}^2} + \Gamma(\tilde{T} + \Gamma_c \tilde{T}^2), \quad (12)$$

$$\begin{aligned}
& \tilde{u} \frac{\partial \tilde{T}}{\partial \tilde{x}} + \tilde{v} \frac{\partial \tilde{T}}{\partial \tilde{y}} + \alpha_1 \left(\tilde{u} \frac{\partial \tilde{u}}{\partial \tilde{x}} \frac{\partial \tilde{T}}{\partial \tilde{x}} + \tilde{v} \frac{\partial \tilde{v}}{\partial \tilde{y}} \frac{\partial \tilde{T}}{\partial \tilde{y}} + \tilde{v} \frac{\partial \tilde{u}}{\partial \tilde{y}} \frac{\partial \tilde{T}}{\partial \tilde{x}} + \tilde{u} \frac{\partial \tilde{v}}{\partial \tilde{x}} \frac{\partial \tilde{T}}{\partial \tilde{y}} + 2\tilde{u}\tilde{v} \frac{\partial^2 \tilde{T}}{\partial \tilde{y}\partial \tilde{x}} + \tilde{u}^2 \frac{\partial^2 \tilde{T}}{\partial \tilde{x}^2} \right. \\
& \quad \left. + \tilde{v}^2 \frac{\partial^2 \tilde{T}}{\partial \tilde{y}^2} \right) \\
& = \frac{1}{\gamma} \frac{\partial}{\partial \tilde{y}} \left[(1 + \epsilon \tilde{T}) \frac{\partial \tilde{T}}{\partial \tilde{y}} \right] + \frac{\eta}{\gamma} \left[-4 \frac{\partial^2 \tilde{T}}{\partial \tilde{y}^2} + \frac{3}{(\tilde{T}_s - 1)} \frac{\partial^2}{\partial \tilde{y}^2} \{1 + (\tilde{T}_s - 1)\tilde{T}\}^2 \right] \\
& + \xi \tilde{T},
\end{aligned} \tag{13}$$

Where α represents the Deborah number, Γ indicates the mixed convection parameter, Gr indicates the thermal Grashof number, \Re represents the Reynolds number, Γ_c represents the nonlinear convection parameter, α_1 indicates the non-Fourier Deborah number, γ indicates the Prandtl number, ξ indicates the heat source/sink parameter, $\tilde{T}_s > 1$ indicates the temperature ratio parameter and η indicates the thermal radiation parameter. The following are the definitions of the dimensionless variables:

$$\begin{aligned}
\alpha = Ms, \Gamma = \frac{Gr}{\Re^2}, Gr = \frac{g\beta(T - T_{amb})x^3}{\nu^2}, \Re = \frac{sx}{\nu}, \Gamma_c = \frac{\beta_1}{\beta}(T - T_{amb}), \alpha_1 = N_f s, \gamma \\
= \frac{(\rho C_p)\nu}{\kappa_{amb}}, \xi = \frac{Q}{\rho c_1 C_p}, \eta = \frac{8\sigma^* T_{amb}^3}{3\kappa_{amb} k^*}.
\end{aligned} \tag{14}$$

The boundary conditions in dimensionless form are defined as:

$$\tilde{u} = \tilde{x}, \tilde{v} = 0, \tilde{T} = 1 \quad \text{at} \quad \tilde{y} = 0, \tag{15}$$

$$\tilde{u} \rightarrow 0, \tilde{T} \rightarrow 0 \quad \text{as} \quad \tilde{y} \rightarrow \infty. \tag{16}$$

3. Implementation of Lie Symmetry transformations

Defining a stream function $\tilde{\Phi}$ to satisfy the governing continuity equation for the dimensionless equations (12)-(16), as follows:

$$\tilde{u} = \frac{\partial \tilde{\Phi}}{\partial \tilde{y}}, \tilde{v} = -\frac{\partial \tilde{\Phi}}{\partial \tilde{x}}. \tag{17}$$

By virtue of Eqn. (17), then Eqns. (12)-(16) emerge as:

$$\begin{aligned}
& \frac{\partial \tilde{\Phi}}{\partial \tilde{y}} \frac{\partial^2 \tilde{\Phi}}{\partial \tilde{x}\partial \tilde{y}} - \frac{\partial \tilde{\Phi}}{\partial \tilde{x}} \frac{\partial^2 \tilde{\Phi}}{\partial \tilde{y}^2} + \alpha \left[\left(\frac{\partial \tilde{\Phi}}{\partial \tilde{y}} \right)^2 \frac{\partial^3 \tilde{\Phi}}{\partial \tilde{x}^2 \partial \tilde{y}} + \left(\frac{\partial \tilde{\Phi}}{\partial \tilde{x}} \right)^2 \frac{\partial^3 \tilde{\Phi}}{\partial \tilde{y}^3} - 2 \frac{\partial \tilde{\Phi}}{\partial \tilde{y}} \frac{\partial \tilde{\Phi}}{\partial \tilde{x}} \frac{\partial^3 \tilde{\Phi}}{\partial \tilde{x}\partial \tilde{y}^2} \right] \\
& = \frac{\partial^3 \tilde{\Phi}}{\partial \tilde{y}^3} + \Gamma(\tilde{T} + \Gamma_c \tilde{T}^2).
\end{aligned} \tag{18}$$

$$\begin{aligned}
& \frac{\partial \tilde{\Phi}}{\partial \tilde{y}} \frac{\partial \tilde{T}}{\partial \tilde{x}} - \frac{\partial \tilde{\Phi}}{\partial \tilde{x}} \frac{\partial \tilde{T}}{\partial \tilde{y}} \\
& + \alpha_1 \left[\frac{\partial \tilde{\Phi}}{\partial \tilde{y}} \frac{\partial^2 \tilde{\Phi}}{\partial \tilde{x} \partial \tilde{y}} \frac{\partial \tilde{T}}{\partial \tilde{x}} + \frac{\partial \tilde{\Phi}}{\partial \tilde{x}} \frac{\partial^2 \tilde{\Phi}}{\partial \tilde{x} \partial \tilde{y}} \frac{\partial \tilde{T}}{\partial \tilde{y}} - \frac{\partial \tilde{\Phi}}{\partial \tilde{x}} \frac{\partial^2 \tilde{\Phi}}{\partial \tilde{y}^2} \frac{\partial \tilde{T}}{\partial \tilde{x}} - \frac{\partial \tilde{\Phi}}{\partial \tilde{y}} \frac{\partial^2 \tilde{\Phi}}{\partial \tilde{x}^2} \frac{\partial \tilde{T}}{\partial \tilde{y}} \right. \\
& \left. - 2 \frac{\partial \tilde{\Phi}}{\partial \tilde{y}} \frac{\partial \tilde{\Phi}}{\partial \tilde{x}} \frac{\partial^2 \tilde{T}}{\partial \tilde{y} \partial \tilde{x}} + \left(\frac{\partial \tilde{\Phi}}{\partial \tilde{y}} \right)^2 \frac{\partial^2 \tilde{T}}{\partial \tilde{x}^2} + \left(\frac{\partial \tilde{\Phi}}{\partial \tilde{x}} \right)^2 \frac{\partial^2 \tilde{T}}{\partial \tilde{y}^2} \right] \\
& = \frac{1}{\gamma} \frac{\partial}{\partial \tilde{y}} \left[(1 + \epsilon \tilde{T}) \frac{\partial \tilde{T}}{\partial \tilde{y}} \right] + \frac{\eta}{\gamma} \left[-4 \frac{\partial^2 \tilde{T}}{\partial \tilde{y}^2} + \frac{3}{(\tilde{T}_s - 1)} \frac{\partial^2}{\partial \tilde{y}^2} \{1 + (\tilde{T}_s - 1) \tilde{T}\}^2 \right] \\
& + \xi \tilde{T}.
\end{aligned} \tag{19}$$

The boundary conditions become:

$$\frac{\partial \tilde{\Phi}}{\partial \tilde{y}} = \tilde{x}, -\frac{\partial \tilde{\Phi}}{\partial \tilde{x}} = 0, \tilde{T} = 1 \quad \text{at} \quad \tilde{y} = 0, \tag{20}$$

$$\frac{\partial \tilde{\Phi}}{\partial \tilde{y}} \rightarrow 0, \tilde{T} \rightarrow 0 \quad \text{as} \quad \tilde{y} \rightarrow \infty. \tag{21}$$

3.1 Transformation of scaling group

For the formulated equations, we assume the following form of Lie group transformations:

$$\chi: \{x = \tilde{x}e^{\epsilon a}, y = \tilde{y}e^{\epsilon b}, T = \tilde{T}e^{\epsilon c}, \Phi = \tilde{\Phi}e^{\epsilon d}, \tag{22}$$

Where ϵ represents the group parameter, a, b, c, d are the real numbers which will be determined later. The above equation (22) represents the point transformations $\tilde{x}, \tilde{y}, \tilde{T}, \tilde{\Phi}$ to x, y, T, Φ . Assuming Eqns. (18) – (21) are *invariant* under the given transformation χ . Therefore, Eqns. (18) and (19) become:

$$\begin{aligned}
& e^{\epsilon(a-2d+2b)} \left(\frac{\partial \Phi}{\partial y} \frac{\partial^2 \Phi}{\partial x \partial y} - \frac{\partial \Phi}{\partial x} \frac{\partial^2 \Phi}{\partial y^2} \right) \\
& + \alpha e^{\epsilon(2a-3d+3b)} \left[\left(\frac{\partial \Phi}{\partial y} \right)^2 \frac{\partial^3 \Phi}{\partial x^2 \partial y} + \left(\frac{\partial \Phi}{\partial x} \right)^2 \frac{\partial^3 \Phi}{\partial y^3} - 2 \frac{\partial \Phi}{\partial y} \frac{\partial \Phi}{\partial x} \frac{\partial^3 \Phi}{\partial x \partial y^2} \right] \\
& = e^{\epsilon(-d+3b)} \frac{\partial^3 \Phi}{\partial y^3} + \Gamma (e^{-\epsilon c} \tilde{T} + e^{-2\epsilon c} \Gamma_c \tilde{T}^2).
\end{aligned} \tag{23}$$

$$\begin{aligned}
& e^{\varepsilon(a-d-c+b)} \left(\frac{\partial \Phi}{\partial y} \frac{\partial T}{\partial x} - \frac{\partial \Phi}{\partial x} \frac{\partial T}{\partial y} \right) \\
& + \alpha_1 e^{\varepsilon(2a-2d-c+2b)} \left(\frac{\partial \Phi}{\partial y} \frac{\partial^2 \Phi}{\partial x \partial y} \frac{\partial T}{\partial x} + \frac{\partial \Phi}{\partial x} \frac{\partial^2 \Phi}{\partial x \partial y} \frac{\partial T}{\partial y} - \frac{\partial \Phi}{\partial x} \frac{\partial^2 \Phi}{\partial y^2} \frac{\partial T}{\partial x} \right. \\
& \left. - \frac{\partial \Phi}{\partial y} \frac{\partial^2 \Phi}{\partial x^2} \frac{\partial T}{\partial y} - 2 \frac{\partial \Phi}{\partial y} \frac{\partial \Phi}{\partial x} \frac{\partial^2 T}{\partial x \partial y} + \left(\frac{\partial \Phi}{\partial y} \right)^2 \frac{\partial^2 T}{\partial x^2} + \left(\frac{\partial \Phi}{\partial x} \right)^2 \frac{\partial^2 T}{\partial y^2} \right) \\
& = \frac{1}{\gamma} \left[e^{\varepsilon(2b-c)} \frac{\partial^2 T}{\partial y^2} + \varepsilon e^{2\varepsilon(b-c)} \left(\frac{\partial T}{\partial y} \right)^2 + \varepsilon e^{2\varepsilon(b-c)} T \frac{\partial^2 T}{\partial y^2} \right] \\
& + \frac{\eta}{\gamma} \left[-4e^{\varepsilon(2b-c)} \frac{\partial^2 T}{\partial y^2} \right. \\
& \left. + 6 \left(e^{\varepsilon(2b-c)} \frac{\partial^2 T}{\partial y^2} + (\tilde{T}_s - 1) e^{2\varepsilon(b-c)} \left(\frac{\partial T}{\partial y} \right)^2 + (\tilde{T}_s - 1) e^{2\varepsilon(b-c)} T \frac{\partial^2 T}{\partial y^2} \right) \right] \\
& + e^{-c\varepsilon} \xi T. \tag{24}
\end{aligned}$$

The boundary conditions (20) and (21) become:

$$e^{\varepsilon(b-d)} \frac{\partial \Phi}{\partial y} = e^{-a\varepsilon} \tilde{\chi}, e^{\varepsilon(a-d)} \frac{\partial \Phi}{\partial x} = 0, e^{-c\varepsilon} T = 1 \quad \text{at } y = 0, \tag{25}$$

$$e^{\varepsilon(b-d)} \frac{\partial \Phi}{\partial y} \rightarrow 0, e^{-c\varepsilon} T \rightarrow 0 \quad \text{as } y \rightarrow \infty. \tag{26}$$

Using the *invariance condition* shows the following relationships between the parameters:

$$\left. \begin{aligned}
a - 2d + 2b &= 2a - 3d + 3b = 3b - d = -c = -2c, \\
a - d - c + b &= 2a - 2d - c + 2b = 2b - c = 2(b - c) = -c, \\
b - d &= -a, -c = 0, a - d = 0,
\end{aligned} \right\} \tag{27}$$

Solving the above set of equations, leads to:

$$a = d, b = c = 0. \tag{28}$$

Invoking the above equation (28) into equation (22), gives:

$$\chi: \{x = \tilde{x}e^{\varepsilon a}, y = \tilde{y}, T = \tilde{T}, \Phi = \tilde{\Phi}e^{\varepsilon a}, \tag{29}$$

The terms in the above equation can be expanded in terms of a Taylor series, and ignoring higher powers of ε we have:

$$\chi: \{x = \tilde{x}(1 + \varepsilon a), y - \tilde{y} = 0, T - \tilde{T} = 0, \Phi = \tilde{\Phi}(1 + \varepsilon a), \tag{30}$$

and

$$\frac{d\tilde{x}}{a\tilde{x}} = \frac{d\tilde{y}}{0} = \frac{d\tilde{T}}{0} = \frac{d\tilde{\Phi}}{a\tilde{\Phi}}, \tag{31}$$

After solving the above system, we obtained the following solutions:

$$\tilde{y} = \zeta, \tilde{\Phi} = \tilde{x}h(\zeta), \tilde{T} = T(\zeta),$$

(32)

Invoking equation (32) into equation (18-21) yields the following self-similar ordinary differential equations for momentum and energy conservation:

$$h''' - \alpha(h^2 h''' - 2h' h h'') + h h'' - h'^2 + \Gamma(T + \Gamma_c T^2) = 0, \quad (33)$$

$$(1 + \epsilon T)T'' + \epsilon T'^2 + \eta[2T'' + 6\{(\tilde{T}_s - 1)T'^2 + (\tilde{T}_s - 1)TT''\}] + \gamma \xi T - \gamma \alpha_1(hh'T' + h^2 T'') + \gamma h T' = 0, \quad (34)$$

The wall and freestream boundary conditions now assume the following form:

$$h' = 1, h = 0, T = 1 \quad \text{at} \quad \zeta = 0, \quad (35)$$

$$h' \rightarrow 0, T \rightarrow 0 \quad \text{as} \quad \zeta \rightarrow \infty. \quad (36)$$

Important wall characteristics in materials coating systems are the *skin friction coefficient* and the *Nusselt number*. These are defined as follows for the Maxwell fluid and quadratic thermal radiation, respectively:

$$S_x = -\frac{2\varrho}{\rho(sx)^2}, N_x = -\left(\frac{x\Xi}{(T_s - T_{\text{amb}})} + q\right)\Big|_{y=0}, \quad (37)$$

In Eqn. (37), the following definitions apply:

$$\varrho = \left[\mu \frac{\partial u}{\partial y} - M \left(2uv \frac{\partial u}{\partial x} + v^2 \frac{\partial u}{\partial y}\right)\right]_{y=0}, \Xi = \kappa(T) \frac{\partial T}{\partial y}, \quad (38)$$

Where $\kappa(T)$ and q have been defined earlier in Eqns. (4)-(5). The associated non-dimensional version of Eqn. (37) can be expressed as:

$$\frac{\sqrt{\Re} S_x}{2} = -[h''(\zeta) - \alpha(h^2(\zeta)h''(\zeta) - 2h(\zeta)h'^2(\zeta))]_{\zeta=0},$$

$$\frac{N_x}{\sqrt{\Re}} = -\left[(1 + \epsilon T(\zeta))T'(\zeta) + \eta[2T'(\zeta) + 6(\tilde{T}_s - 1)T(\zeta)T'(\zeta)]\right]_{\zeta=0}. \quad (39)$$

The parameters $\Re, \alpha, \eta, \tilde{T}_s, \epsilon$ in the above equation have been defined in Eqn. (14).

4. Numerical solution of nonlinear non-Fourier coating flow problem

The spectral relaxation technique (SRM) is used to solve the nonlinear coupled differential equations (33)-(34) subjected to boundary conditions (35) and (36).

4.1 The SRM Technique:

The SRM technique can be applied on the governing system of differential equations by reducing the order of Equation (33). We suppose $h' = k$, then Equations (33)-(34) reduce to:

$$k'' - \alpha(h^2 k'' - 2h k k') + h k' - k^2 + \Gamma(T + \Gamma_c T^2) = 0, \quad (37)$$

$$(1 + \epsilon T)T'' + \epsilon T'^2 + \eta(2T'' + 6\{(\tilde{T}_s - 1)T'^2 + (\tilde{T}_s - 1)TT''\}) + \gamma \xi T - \gamma \alpha_1(hkT' + h^2T'') + \gamma hT' = 0, \quad (38)$$

Now, we apply the Gauss–Seidel relaxation scheme to decouple the reduced system as follows:

$$h'_{t+1} = k_t, \quad (39)$$

$$k''_{t+1} + h_t k'_{t+1} = k_t^2 + \alpha(h_t^2 k_t'' - 2h_t k_t k_t'') - \Gamma(T_t + \Gamma_c T_t^2), \quad (40)$$

$$(1 + 2\eta - \gamma \alpha_1 h_{t+1}^2)T''_{t+1} + \gamma h_{t+1} T'_{t+1} - \gamma \alpha_1 h_{t+1} k_{t+1} T'_{t+1} + \gamma \xi T_{t+1} = -\epsilon T_t T''_t - \epsilon T_t'^2 - 6\eta(\tilde{T}_s - 1)T_t'^2 - 6\eta(\tilde{T}_s - 1)T_t T''_t, \quad (41)$$

The corresponding boundary conditions emerge as:

$$k_{t+1}(0) = 1, h_{t+1}(0) = 0, T_{t+1}(0) = 1, \quad (42)$$

$$k_{t+1}(\infty) \rightarrow 0, T_{t+1}(\infty) \rightarrow 0. \quad (43)$$

Here the terms with subscripts “ $t + 1$ ” indicate the *current* approximated numerics, and the terms with subscripts “ t ” correspond to *previous* approximated numerics.

The set of linearized Eqns. (39)-(41) dependent upon boundary conditions (42)-(43) are solved utilizing the *Chebyshev pseudo-spectral method* [45]. Accordingly, the actual area $[0, \infty]$ is converted to finite length $[0, L]$, where L is elected to be sufficiently large. The converted domain is changed to $[-1, 1]$ by utilizing the transformation, $\zeta = 2\zeta/L$, and the nodal points among -1 up to 1 are characterized as $\zeta_j = \text{Cos}(\pi_j)$, $j = 0, 1, 2, \dots, N$, which are known as Gauss-Lobatto collocation points. This technique depends on $[\mathbf{D}]$, the differentiation matrix which can be approximated in various ways. Here $[\mathbf{D}]$ is processed following Trefethen [46]. Now, the system of Eqns. (39)-(43) becomes:

$$\mathbf{D}h_{t+1} = k_t, \quad (44)$$

$$\{\mathbf{D}^2 + \text{diag}[a_{0,t}]\mathbf{D}\}k_{t+1} = C_{1,t}, \quad (45)$$

$$[(1 + \eta - \gamma \alpha_1 \text{diag}[h_{t+1}^2])\mathbf{D}^2 + \gamma \text{diag}[h_{t+1}]\mathbf{D} - (\gamma \alpha_1 \text{diag}[h_{t+1}]\text{diag}[k_{t+1}]\mathbf{D} - \gamma \xi \mathbf{I})]T_{t+1} = C_{2,t}, \quad (46)$$

The related boundary conditions have the form:

$$k_{t+1}(\zeta_N) = 1, h_{t+1}(\zeta_N) = 0, T_{t+1}(\zeta_N) = 1, \quad (47)$$

$$k_{t+1}(\zeta_0) \rightarrow 0, T_{t+1}(\zeta_0) \rightarrow 0, \quad (48)$$

Now, construct the compressed form for Eqns. (44)-(46) as follows:

$$\ddot{A}_{11}h_{t+1} = \ddot{E}_{11}, \quad (49)$$

$$\ddot{A}_{22}k_{t+1} = \ddot{E}_{22}, \quad (50)$$

$$\ddot{A}_{33}T_{t+1} = \ddot{E}_{33}, \quad (51)$$

Where

$$\ddot{A}_{11} = \mathbf{D}, \ddot{E}_{11} = k_t, \quad (52)$$

$$\ddot{A}_{22} = \mathbf{D}^2 + \text{diag}[a_{0,t}]\mathbf{D}, \ddot{E}_{22} = C_{1,t}, \quad (53)$$

$$\begin{aligned} \ddot{A}_{33} = & (1 + \eta - \gamma\alpha_1 \text{diag}[h_{t+1}^2])\mathbf{D}^2 + \gamma \text{diag}[h_{t+1}]\mathbf{D} \\ & - (\gamma\alpha_1 \text{diag}[h_{t+1}]\text{diag}[k_{t+1}]\mathbf{D} - \gamma\xi\mathbf{I}), \ddot{E}_{33} = C_{2,t}. \end{aligned} \quad (54)$$

Here the following notation applies:

$$\left. \begin{aligned} a_{0,s} &= h_t, \\ C_{1,t} &= -k_t^2 + \alpha(k_t^2 k_t'' - 2h_t k_t k_t'') + \Gamma(T_t + \Gamma_c T_t^2), \\ C_{2,t} &= -\epsilon T_t T_t'' - \epsilon T_t'^2 - 6\eta(\tilde{T}_s - 1)T_t'^2 - 6\eta(\tilde{T}_s - 1)T_t T_t'' \end{aligned} \right\} \quad (55)$$

And

$$\left. \begin{aligned} \text{diag}[a_{0,s}] &= \begin{bmatrix} a_{0,t}(\zeta_0) & \dots & \\ \vdots & \ddots & \vdots \\ & \dots & a_{0,t}(\zeta_N) \end{bmatrix}, \text{diag}[h_{t+1}^2] = \begin{bmatrix} h_{t+1}^2(\zeta_0) & \dots & \\ \vdots & \ddots & \vdots \\ & \dots & h_{t+1}^2(\zeta_N) \end{bmatrix}, \\ \text{diag}[h_{t+1}] &= \begin{bmatrix} h_{t+1}(\zeta_0) & \dots & \\ \vdots & \ddots & \vdots \\ & \dots & h_{t+1}(\zeta_N) \end{bmatrix}, \text{diag}[k_{t+1}] = \begin{bmatrix} k_{t+1}(\zeta_0) & \dots & \\ \vdots & \ddots & \vdots \\ & \dots & k_{t+1}(\zeta_N) \end{bmatrix} \end{aligned} \right) \quad (56)$$

$h_{t+1} = [h(\zeta_0), h(\zeta_1), \dots, h(\zeta_N)]^T$, $k_{t+1} = [k(\zeta_0), k(\zeta_1), \dots, k(\zeta_N)]^T$, $T_{t+1} = [T(\zeta_0), T(\zeta_1), \dots, T(\zeta_N)]^T$ are vectors of dimensions $(N+1) \times 1$. $\mathbf{0}$ the vector of dimension $(N+1) \times 1$ and \mathbf{I} describes the identity matrices of dimension $(N+1) \times (N+1)$.

The enforcement of boundary conditions on Eqns. (49)-(51) are as below:

$$\left. \begin{aligned} \ddot{A}_{11} &= \begin{bmatrix} \ddot{A}_{11} & \\ \mathbf{0} & \dots & \mathbf{1} \end{bmatrix}, h_{t+1} = \begin{bmatrix} h_{t+1}(\zeta_0) \\ h_{t+1}(\zeta_1) \\ \vdots \\ h_{t+1}(\zeta_N) \end{bmatrix}, \ddot{E}_{11} = \begin{bmatrix} \ddot{E}_{11} \\ \mathbf{0} \end{bmatrix}, \ddot{A}_{22} = \begin{bmatrix} \mathbf{1} & \dots & \mathbf{0} \\ & \ddot{A}_{22} & \\ \mathbf{0} & \dots & \mathbf{1} \end{bmatrix}, k_{t+1} = \begin{bmatrix} k_{t+1}(\zeta_0) \\ k_{t+1}(\zeta_1) \\ \vdots \\ k_{t+1}(\zeta_N) \end{bmatrix}, \\ \ddot{E}_{22} &= \begin{bmatrix} \mathbf{0} \\ \ddot{E}_{22} \\ \mathbf{1} \end{bmatrix}, \ddot{A}_{33} = \begin{bmatrix} \mathbf{1} & \dots & \mathbf{0} \\ & \ddot{A}_{33} & \\ \mathbf{0} & \dots & \mathbf{1} \end{bmatrix}, T_{t+1} = \begin{bmatrix} T_{t+1}(\zeta_0) \\ T_{t+1}(\zeta_1) \\ \vdots \\ T_{t+1}(\zeta_N) \end{bmatrix}, \ddot{E}_{33} = \begin{bmatrix} \mathbf{0} \\ \ddot{E}_{33} \\ \mathbf{1} \end{bmatrix}. \end{aligned} \right) \quad (57)$$

The pertinent initial approximations are chosen as below:

$$h_0(\zeta) = (1 - e^{-\zeta}), k_0(\zeta) = e^{-\zeta}, T_0(\zeta) = e^{-\zeta}. \quad (58)$$

The above assumptions obey the boundary conditions (42)-(43) and subsequently the approximated values of h_t, k_t, T_t for each $t = 1, 2, \dots$ are computed by applying the SRM scheme.

5. Numerical results and discussion

This section discusses the graphical and SRM numerical results for various physical parameters. We selected the following parametric values in Matlab to execute the numerical simulations: $\alpha_1 = \Gamma = \Gamma_c = 0.5, \epsilon = 0.3, \xi = 0.1, \eta = 1, \tilde{T}_s = 1.2, \alpha = 0.4, \gamma = 5$. This data corresponds to physically viable non-Newtonian coating materials with appropriate thermal characteristics [28-30]. The graphical results are presented for velocity and thermal profile against numerous values of Deborah number α , mixed convection parameter Γ , nonlinear convection parameter Γ_c , non-Fourier Deborah number α_1 , Prandtl number γ , heat source/sink parameter ξ , and nonlinear thermal radiation η .

5.1 Tabular results:

Tables 1–3 show the numerical computations of skin friction and Nusselt number versus various physical factors. **Table 1** compares numerical findings derived by Sadeghy *et al.* [47] and Abel *et al.* [48] for various values of Deborah number α and the exclusion of convection (mixed and nonlinear) $\Gamma = \Gamma_c = 0$. **Table 2** compares the Nusselt number to prior results obtained by Khan and Pop [49] for different values of Prandtl number γ , whereas the remaining parameters are absent. such as $\Gamma = \Gamma_c = 0, \xi = 0, \alpha_1 = 0, \eta = 0$. Tables 1 and 2 show that the current SRM solutions correlate very closely with previous studies. Confidence in the accuracy of the SRM results is therefore justified. **Table 3** shows the skin friction and Nusselt number for each physical parameter. With increment in mixed convection parameter Γ and the nonlinear convection parameter, Γ_c we can observe that the Nusselt number and skin friction coefficient diminish. However, skin friction and Nusselt number are conversely greatly elevated with increment in Deborah number (α). Increasing nonlinear thermal radiation parameter suppresses Nusselt number whereas the reverse tendency has been found for larger values of Prandtl number and non-Fourier Deborah number (α_1). It is important to mention that when the heat flux is reversed, the Nusselt number can become negative. It is also associated with negative (convective) heat transfer coefficient, and it arises in non-Fourier transport phenomena problems. Negative friction factor implies that flow reversal has occurred in the boundary layer and the shear stress is reversed.

Table 1: Numerical comparison of Skin friction with previous results by assuming $\Gamma = \Gamma_c = 0$.

α	$\sqrt{\Re} S_x / 2$		
	Sadeghy <i>et al.</i> [47]	Abel <i>et al.</i> [48]	Present results
0.0	1.0000	0.9999	1.0000
0.2	1.0549	1.0519	1.0561
0.4	1.1008	1.1018	1.1018
0.8	1.1987	1.1966	1.1966

Table 2: Numerical comparison of Nusselt number with previous results by assuming $\Gamma = \Gamma_c = 0, \xi = 0, \alpha_1 = 0, \eta = 0$.

γ	$N_x/\sqrt{\Re}$	
	Khan and Pop [49]	Present results
0.07	0.0663	0.0663
0.70	0.4539	0.4539
2.0	0.9113	0.9113

Table 3: Numerical values computed from SRM for Skin friction and Nusselt number.

Γ	Γ_c	α	α_1	ϵ	η	γ	ξ	$\sqrt{\Re}S_x/2$	$N_x/\sqrt{\Re}$
0								1.261798	1.667957
0.5								0.495087	1.281993
1								-0.271623	0.860913
	0							0.418114	1.144413
	0.5							0.188201	1.051177
	1							-0.04171	0.956676
		1						-0.009825	1.101789
		1.4						0.199613	1.283379
		2						0.513771	1.539202
			0						0.965805
			0.2						1.088774
			0.4						1.216068
				0					1.580577
				0.5					1.052457
				1					0.371936
					1				1.281993
					1.7				0.182247
					2				-0.37462
						3.5			0.323143
						4			0.663405
						5			1.281993
							-0.6		4.37814
							0		1.83739
							0.3		-0.04534

5.2 Velocity profile:

Figure 2 shows the effects of Deborah number on velocity profile. This figure indicates that higher values of Deborah number significantly oppose the fluid motion. Deborah number represents the elastic effects relative to viscous effects i.e., greater elastic impact decelerates the flow and enhances the thickness of momentum boundary layer. We can see from equation (14) that α is directly proportional to the relaxation time of the viscoelastic parameter. The elastic-viscous material, i.e., the Maxwell fluid model, has a fading memory, which means it preserves the most recent deformation. The greater the impact of relaxation time, the more

dominating the behavior of elastic effects over viscous effects. With larger levels of α , this produces a slowing of the flow. Flow reversal is never triggered; hence velocity magnitudes stay positive at all Deborah number values. For $\alpha = 0$, the results maybe recovered for viscous fluid flow. Figure 3 is plotted to see the variation of mixed convection parameter on velocity profile. We observe that higher values of mixed convection parameter boost the velocity profile. It is clear that thermal buoyancy force is enhanced due to the strong influence of Γ which causes an acceleration in the coating boundary layer flow but a reduction in the thickness of the momentum boundary layer. Figure 4 depicts the effect of the nonlinear convection parameter on the velocity profile. We discovered that the nonlinear convection parameter increases the velocity profile (i.e. accelerates the flow) and decreases the momentum boundary layer thickness. For the strongest case of mixed convection ($\Gamma = 0$), a velocity overshoot is also estimated near the stretching sheet, but it is missing for lesser values of this parameter.

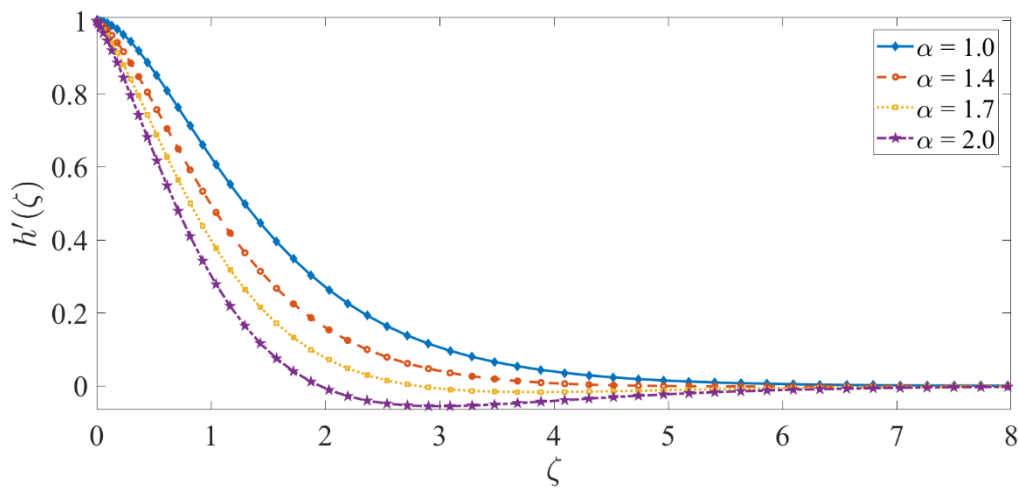


Figure 2: Consequences of Deborah number on velocity profile.

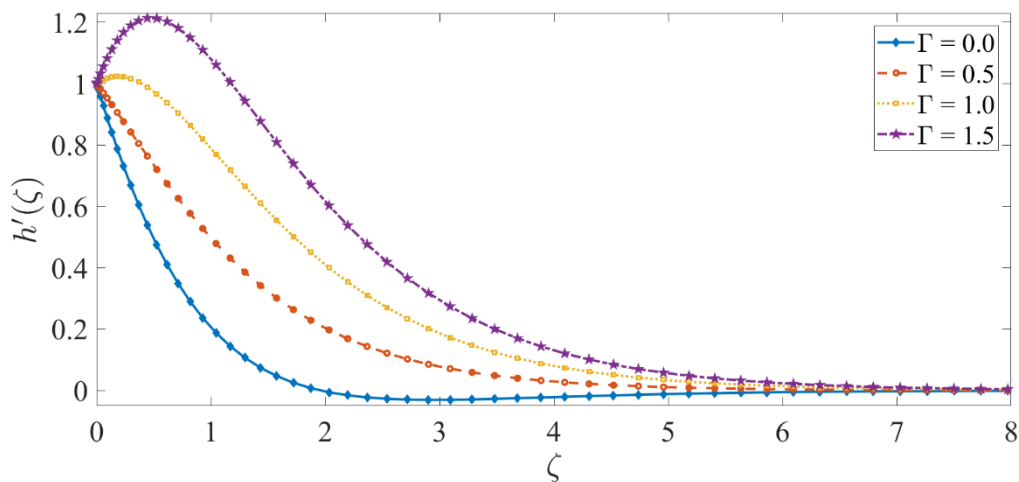


Figure 3: Consequences of mixed convection parameter on velocity profile.

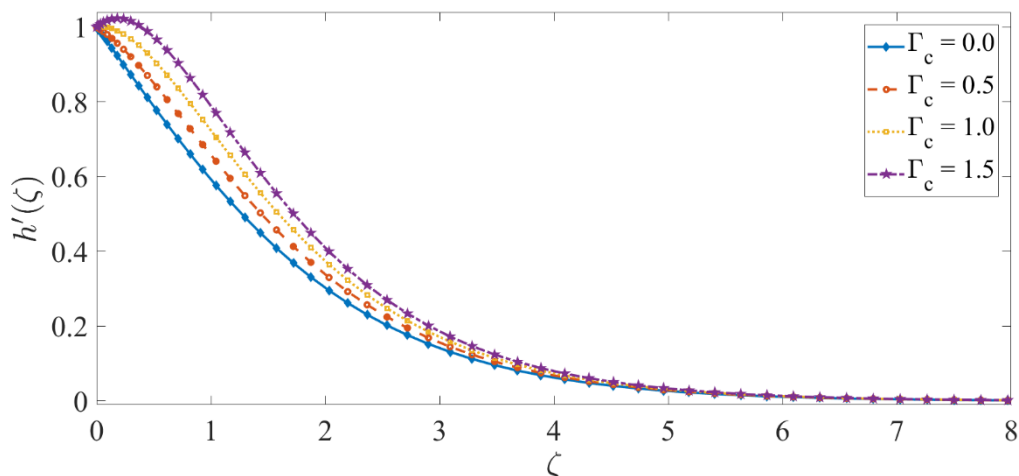


Figure 4: Consequences of nonlinear mixed convection parameter on velocity profile.

5.3 Temperature profile:

Figure 5 shows the behavior of temperature profile for various values of non-Fourier Deborah number. It is noted that increasing values non-Fourier Deborah number remarkably reduces the temperature profile and thermal boundary layer thickness. Furthermore, $\alpha_1 = 0$ corresponds to the classical Fourier case or absence of the effects of non-Fourier Deborah number. A greater heat flux is associated with a lower temperature, while a slower heat flux relaxation time is associated with a higher temperature. With increasing Deborah number values, a greater quantity of heat flux is achieved, resulting in a greater heat transfer rate between the fluid and the wall, and therefore a lower temperature inside the working fluid, i.e., heat is drained from the viscoelastic fluid. Figure 6 shows the behavior ϵ on temperature profile. This parameter describes the attributes of thermal conductivity. We can see in Figure 6 that temperature magnitudes increase significantly, and thermal boundary layer thickness is elevated due to the strong influence of ϵ . Figure 7 shows that the nonlinear thermal radiation parameter increases the thickness of the thermal boundary layer and the temperature profile. As the thermal radiation parameter increases, the radiative flux energizes the polymeric flow, increasing the thermal energy in the regime. Higher thermal radiation levels result in higher temperatures and thicker thermal boundary layers. This effect is maintained at all transverse distances from the stretched sheet. Figure 8 depicts how the mixed convection parameter affects the temperature profile. The mixed convection parameter increases the temperature profile and the thickness of the thermal boundary layer in this image. Figure 9 indicates, however, that the nonlinear mixed convection effects on the temperature profile are comparable to the mixed convection parameter, although a comparatively small temperature boost is generated. Figure 10 shows that a greater Prandtl number lowers temperature values and thermal boundary layer thickness. The Prandtl number defines the rate of momentum diffusion in relation to the rate of heat diffusion in the flow. When the Prandtl number is less than one, the rate of energy diffusion exceeds the rate of momentum diffusion. However, for polymeric non-Newtonian flows, a Prandtl number larger than one is more suitable [50]. Higher values of Prandtl number indicates less impact of thermal conductivity, and therefore, this surpasses the thermal convection and as a result the temperature profile rises. In Figure 11, we can see that when the heat generation parameter increases ($\xi > 0$), the temperature profile significantly increases, and the thickness of the thermal boundary layer rises. However, when heat absorption ($\xi < 0$) is increased, the thermal boundary layer becomes thinner, and the temperature profile diminishes. Physically, the influence of heat generation causes an increment in the fluid

temperature i. e. a heating effect, and heat absorption parameter shows the converse impact i. e. a cooling effect.

It is also worth noting that in all of the plots, asymptotically smooth profiles are estimated in the free stream, showing that the SRM solution prescribes a sufficiently big infinity boundary condition.

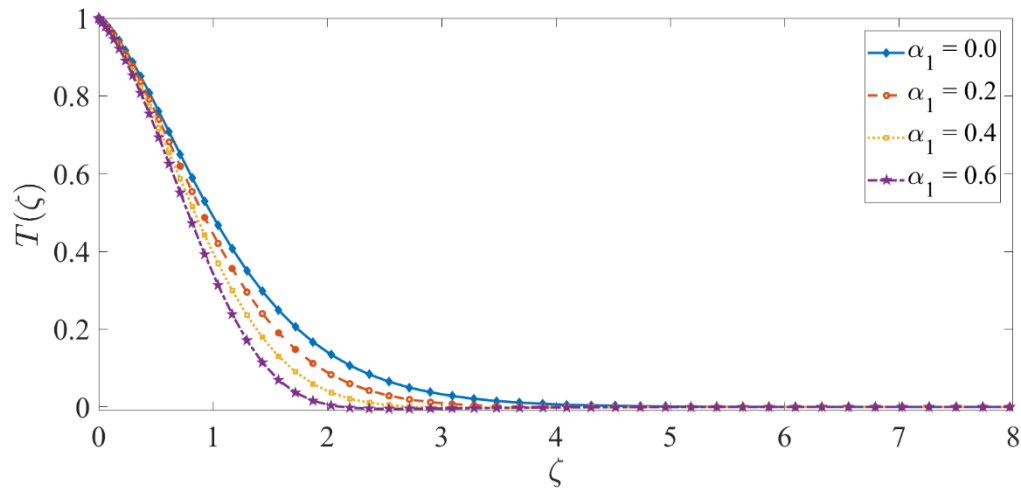


Figure 5: Consequences of thermal relaxation parameter on temperature profile.

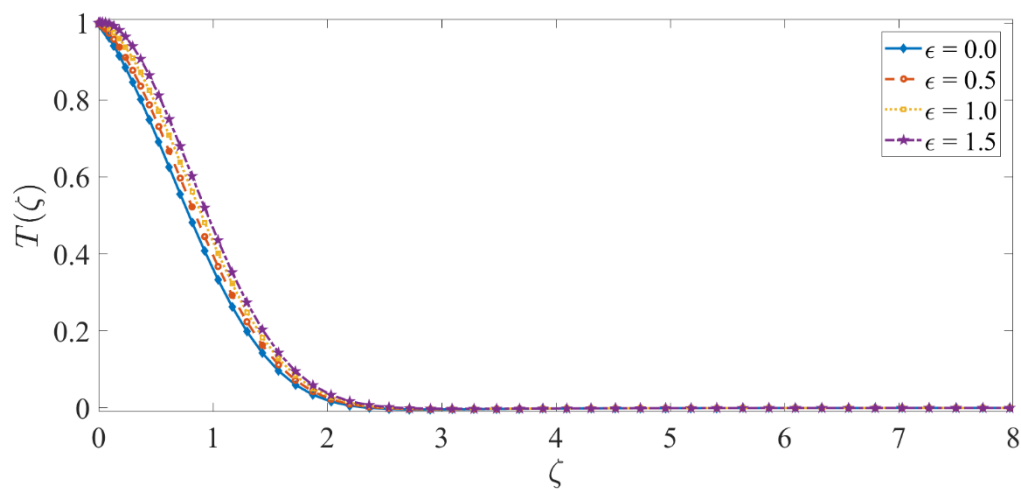


Figure 6: Consequences of attributes of the thermal conductivity on temperature profile.

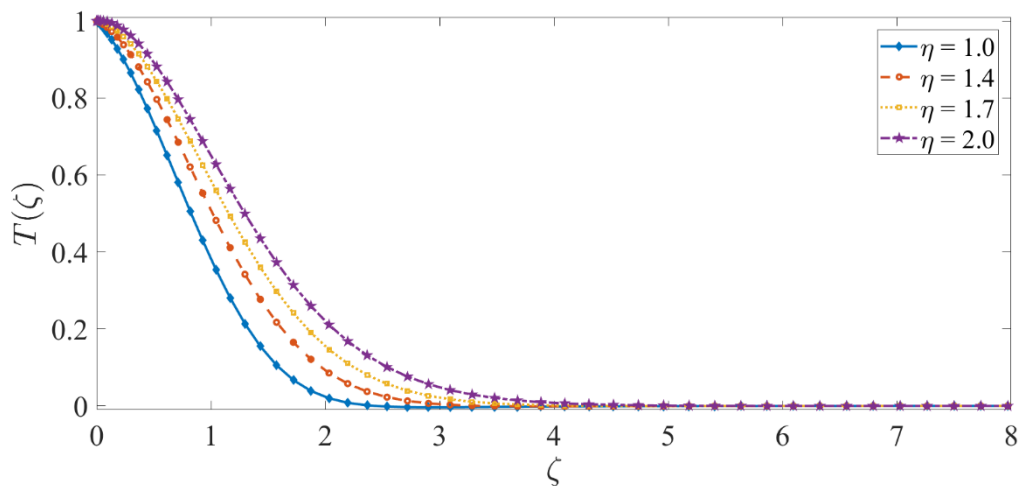


Figure 7: Consequences of thermal radiation on temperature profile.

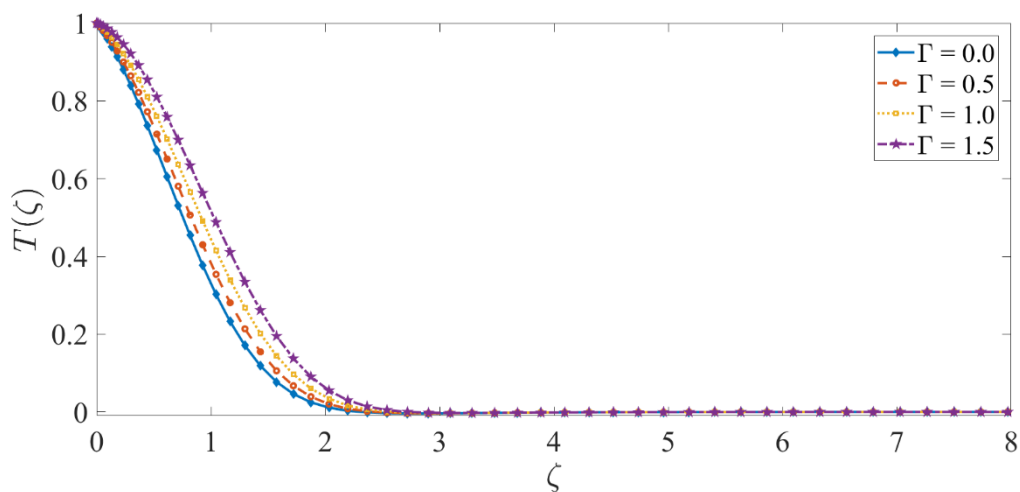


Figure 8: Consequences of mixed convection parameter on temperature profile.

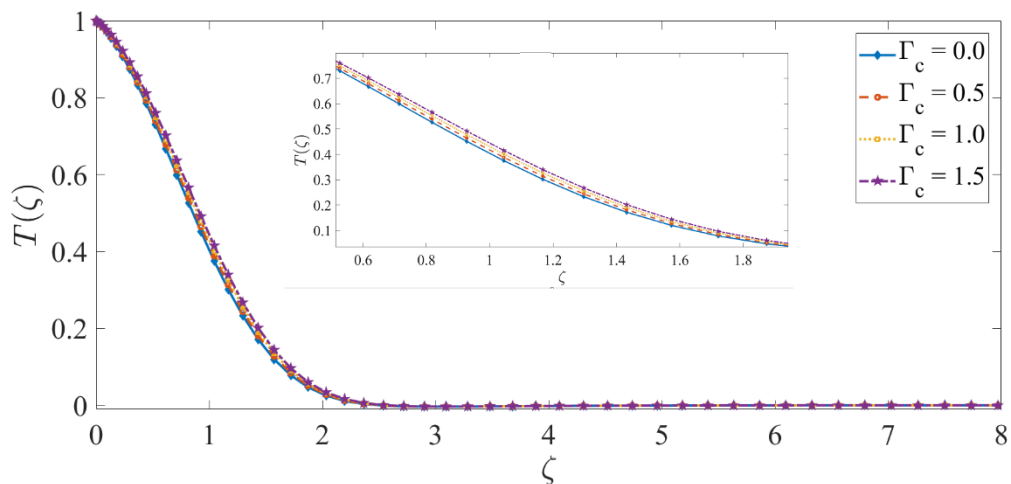


Figure 9: Consequences of nonlinear convection parameter on temperature profile.

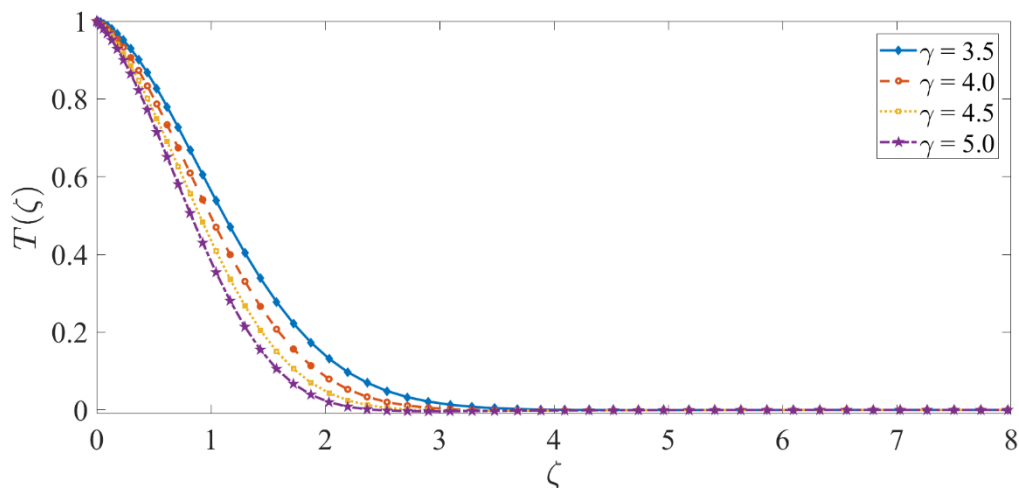


Figure 10: Consequences of Prandtl number on temperature profile.

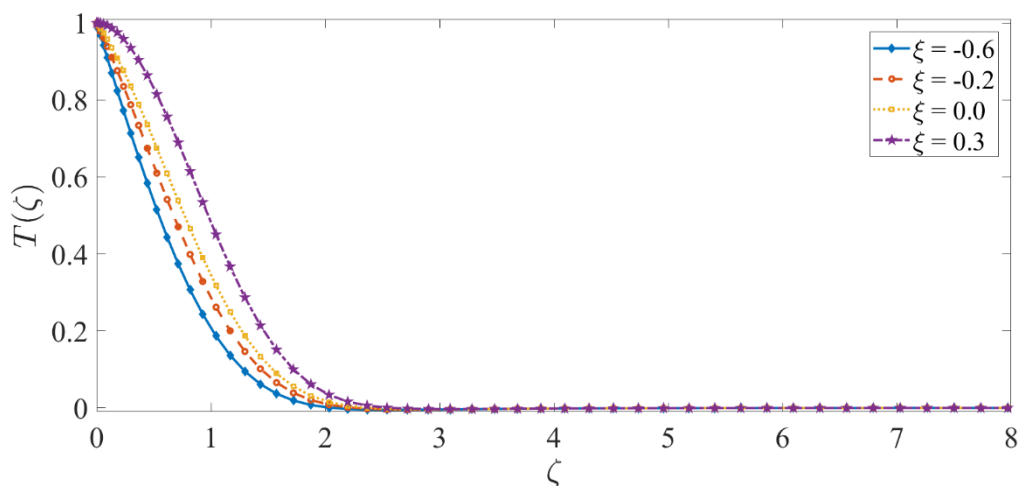


Figure 11: Consequences of heat source/sink on temperature profile.

6. Conclusions

A novel mathematical model for nonlinear quadratic convection and non-Fourier heat flux in incompressible, steady state coating boundary layer flow of a Maxwell elasto-viscous fluid has been devised as a simulation of high-temperature polymer coating manufacturing. Nonlinear quadratic thermal radiation and heat source/sink effects have been considered. Transformations of Lie symmetry have been accomplished. The spectral relaxation approach was used to solve the transformed, dimensionless, nonlinear ordinary differential boundary value problem. Validation with previous studies in the literature has been conducted. The important results are listed below:

- i. Increasing the Deborah number (a Maxwell non-Newtonian parameter) delays the flow but increases the thickness of the momentum boundary layer.
- ii. Elevation in mixed convection and nonlinear convection parameter enhances velocities but reduces momentum boundary layer thickness.

- iii. Increasing the non-Fourier Deborah number, i.e., greater thermal relaxation, causes temperature to fall and the thickness of the thermal boundary layer to decrease.
- iv. Temperature and thermal boundary layer thickness increase when nonlinear thermal radiation, mixed convection, and nonlinear convection parameters are increased.
- v. Temperature is reduced as the Prandtl number and heat sink (absorption) increase, whereas it is increased as the heat source (production) and thermal conductivity parameter increase.
- vi. We found that the present solutions are in close agreement with prior findings for skin friction and Nusselt number, which also validates the published results using SRM.

The present simulations have revealed some interesting features of non-Newtonian high-temperature polymeric coating materials processing. However, attention has been restricted to steady state flows without mass diffusion. Future studies may consider these aspects.

References

- [1] Goren, S. L. (1966). On free convection in water at 4° C. *Chemical Engineering Science*, 21(6-7), 515-518.
- [2] Mahanthesh, B., Animasaun, I. L., Rahimi-Gorji, M., & Alarifi, I. M. (2019). Quadratic convective transport of dusty Casson and dusty Carreau fluids past a stretched surface with nonlinear thermal radiation, convective condition and non-uniform heat source/sink. *Physica A: Statistical Mechanics and its Applications*, 535, 122471.
- [3] Hayat, T., Haider, F., & Alsaedi, A. (2020). Darcy-Forchheimer flow with nonlinear mixed convection. *Applied Mathematics and Mechanics*, 41(11), 1685-1696.
- [4] Reddy, M. G., Vijayakumari, P., Sudharani, M. V. V. N. L., & Kumar, K. G. (2020). Quadratic convective heat transport of Casson nanoliquid over a contract cylinder: an unsteady case. *BioNanoScience*, 10(1), 344-350.
- [5] Akolade, M. T. (2021). Thermophysical impact on the squeezing motion of non-Newtonian fluid with quadratic convection, velocity slip, and convective surface conditions between parallel disks. *Partial differential equations in applied mathematics*, 4, 100056.
- [6] Patil, P. M., Kulkarni, M., & Tonannavar, J. R. (2021). A computational study of the triple-diffusive nonlinear convective nanoliquid flow over a wedge under convective boundary constraints. *International Communications in Heat and Mass Transfer*, 128, 105561.
- [7] Shahid, A., Bhatti, M. M., Anwar Bég, O., Animasaun, I. L., & Javid, K. (2021). Spectral computation of reactive bi-directional hydromagnetic non-Newtonian convection flow from a stretching upper parabolic surface in non-Darcy porous medium. *International Journal of Modern Physics B*, 35(29), 2150294.
- [8] Shaw, S., Samantaray, S. S., Misra, A., Nayak, M. K., & Makinde, O. D. (2022). Hydromagnetic flow and thermal interpretations of Cross hybrid nanofluid influenced by linear, nonlinear and quadratic thermal radiations for any Prandtl number. *International Communications in Heat and Mass Transfer*, 130, 105816.
- [9] Makinde, O. D., & Animasaun, I. L. (2016). Thermophoresis and Brownian motion effects on MHD bioconvection of nanofluid with nonlinear thermal radiation and quartic chemical reaction past an upper horizontal surface of a paraboloid of revolution. *Journal of Molecular liquids*, 221, 733-743.

- [10] Sreedevi, P., Reddy, P. S., & Sheremet, M. (2019). A comparative study of Al₂O₃ and TiO₂ nanofluid flow over a wedge with non-linear thermal radiation. *International Journal of Numerical Methods for Heat & Fluid Flow*, 30(3), 1291-1317.
- [11] Khan, S. U., Tlili, I., Waqas, H., & Imran, M. (2021). Effects of nonlinear thermal radiation and activation energy on modified second-grade nanofluid with Cattaneo–Christov expressions. *Journal of Thermal Analysis and Calorimetry*, 143(2), 1175-1186.
- [12] Khan, W. A., Anjum, N., Waqas, M., Abbas, S. Z., Irfan, M., & Muhammad, T. (2021). Impact of stratification phenomena on a nonlinear radiative flow of sutterby nanofluid. *Journal of Materials Research and Technology*, 15, 306-314.
- [13] Mahanthesh, B., Mackolil, J., Radhika, M., & Al-Kouz, W. (2021). Significance of quadratic thermal radiation and quadratic convection on boundary layer two-phase flow of a dusty nanoliquid past a vertical plate. *International Communications in Heat and Mass Transfer*, 120, 105029.
- [14] Patil, P. M., & Goudar, B. (2022). Entropy generation analysis from the time-dependent quadratic combined convective flow with multiple diffusions and nonlinear thermal radiation. *Chinese Journal of Chemical Engineering*.
<https://doi.org/10.1016/j.cjche.2022.01.013>
- [15] Algehyne, E. A., Aldhabani, M. S., Saeed, A., Dawar, A., & Kumam, P. (2022). Mixed convective flow of Casson and Oldroyd-B fluids through a stratified stretching sheet with nonlinear thermal radiation and chemical reaction. *Journal of Taibah University for Science*, 16(1), 193-203.
- [16] Fourier, J. (1822). *Théorie Analytique de Chaleur*. chez firmin didot, pere et fils. Paris.
- [17] Cattaneo, C. (1948). Sulla conduzione del calore. *Atti Sem. Mat. Fis. Univ. Modena*, 3, 83-101.
- [18] Christov, C. I. (2009). On frame indifferent formulation of the Maxwell–Cattaneo model of finite-speed heat conduction. *Mechanics Research Communications*, 36(4), 481-486.
- [19] Bissell, J. J. (2016). Thermal convection in a magnetized conducting fluid with the Cattaneo–Christov heat-flow model. *Proceedings of the Royal Society A: Mathematical, Physical and Engineering Sciences*, 472(2195), 20160649.
- [20] Layek, G. C., & Pati, N. C. (2017). Bifurcations and chaos in convection taking non-Fourier heat-flux. *Physics Letters A*, 381(41), 3568-3575.
- [21] Mehmood, R., Rana, S., Anwar Bég, O., & Kadir, A. (2018). Numerical study of chemical reaction effects in magnetohydrodynamic Oldroyd-B: oblique stagnation flow with a non-Fourier heat flux model. *Journal of the Brazilian Society of Mechanical Sciences and Engineering*, 40(11), 1-14.
- [22] Shamshuddin, M. D., Mishra, S. R., Bég, O. A., & Kadir, A. (2019). Numerical study of heat transfer and viscous flow in a dual rotating extendable disk system with a non-Fourier heat flux model. *Heat Transfer—Asian Research*, 48(1), 435-459.
- [23] Gangadhar, K., Keziya, K., Kannan, T., & Munjam, S. R. (2020). Analytical investigation on CNT based Maxwell nano-fluid with Cattaneo–Christov heat flux due to thermal radiation. *International Journal of Applied and Computational Mathematics*, 6(4), 1-25.
- [24] Ibrahim, W., & Gadisa, G. (2020). Finite element solution of nonlinear convective flow of Oldroyd-B fluid with Cattaneo-Christov heat flux model over nonlinear stretching sheet with heat generation or absorption. *Propulsion and Power Research*, 9(3), 304-315.
- [25] Khan, S. U., Tlili, I., Waqas, H., & Imran, M. (2021). Effects of nonlinear thermal radiation and activation energy on modified second-grade nanofluid with Cattaneo–Christov expressions. *Journal of Thermal Analysis and Calorimetry*, 143(2), 1175-1186.
- [26] Waqas, H., Khan, S. A., Bhatti, M. M., & Hussain, S. (2021). Bioconvection mechanism using third-grade nanofluid flow with Cattaneo–Christov heat flux model and Arrhenius kinetics. *International Journal of Modern Physics B*, 35(17), 2150178.

- [27]Turkyilmazoglu, M. (2021). Heat transfer enhancement feature of the Non-Fourier Cattaneo–Christov heat flux model. *Journal of Heat Transfer*, 143(9).
- [28]Turkyilmazoglu, M. (2022). Exponential nonuniform wall heating of a square cavity and natural convection. *Chinese Journal of Physics*, 77, 2122-2135.
- [29]Bejawada, S. G., Reddy, Y. D., Jamshed, W., Nisar, K. S., Alharbi, A. N., & Chouikh, R. (2022). Radiation effect on MHD Casson fluid flow over an inclined non-linear surface with chemical reaction in a Forchheimer porous medium. *Alexandria Engineering Journal*, 61(10), 8207-8220.
- [30]Nalivela, N. R., Vempati, S. R., Ravindra Reddy, B., & Dharmendar Reddy, Y. (2022). Viscous dissipation and thermal radiation impact on MHD mass transfer natural convective flow over a stretching sheet. *Proceedings of the Institution of Mechanical Engineers, Part E: Journal of Process Mechanical Engineering*, 09544089221081339.
- [31]Khan, M. I., Khan, S. U., Alhazmi, S. E., Helmi, M. M., El-Zahar, E. R., & Malik, M. Y. (2022). Variable thermal applications of radiative micropolar nanofluid solutal boundary conditions. *Waves in Random and Complex Media*, 1-20.
- [32]S. Chakravorty and C.S. Brown, The significance of thermal material parameters in polymer processing, *NPL Report (UK) DMM (A) 167*, April (1995)
- [33]Jerald A. Britten and Ian M. Thomas, Non-Newtonian flow effects during spin coating large-area optical coatings with colloidal suspensions, *Journal of Applied Physics*, 71, 972 (1992).
- [34]A. Wang *et al.*, High-temperature behaviour of LPCVD ZrB₂ coatings subjected to intense radiative flux, *Surface and Coatings Technology*, 73, 60-65 (1995).
- [35]S. Bose, *High Temperature Coatings*, Elsevier, USA (2007).
- [36]Quentin Flamant and David R. Clarke, Opportunities for minimizing radiative heat transfer in future thermal and environmental barrier coatings, *Scripta Materialia*, 173, 26-31 (2019).
- [37]Hobiny, A., Alzahrani, F., Abbas, I., & Marin, M. (2020). The effect of fractional time derivative of bioheat model in skin tissue induced to laser irradiation. *Symmetry*, 12(4), 602.
- [38]Abouelregal, A. E., & Marin, M. (2020). The size-dependent thermoelastic vibrations of nanobeams subjected to harmonic excitation and rectified sine wave heating. *Mathematics*, 8(7), 1128.
- [39]Mahanthesh, B., Joseph, T. V., & Thriveni, K. (2021). Dynamics of non-Newtonian nanoliquid with quadratic thermal convection. In *Mathematical Fluid Mechanics* (pp. 223-248). De Gruyter.
- [40]Reddy, Y. D., Mebarek-Oudina, F., Goud, B. S., & Ismail, A. I. (2022). Radiation, Velocity and Thermal Slips Effect Toward MHD Boundary Layer Flow Through Heat and Mass Transport of Williamson Nanofluid with Porous Medium. *Arabian Journal for Science and Engineering*, 1-15.
- [41]Kays, W. M., Crawford, M. E., & Weigand, B. (1980). *Convective heat and mass transfer* (Vol. 4). New York: McGraw-Hill.
- [42]Arunachalam, M., & Rajappa, N. R. (1978). Thermal boundary layer in liquid metals with variable thermal conductivity. *Flow, Turbulence and Combustion*, 34(2), 179-187.
- [43]Abdelsalam, S. I., Mekheimer, K. S., & Zaher, A. Z. (2022). Dynamism of a hybrid Casson nanofluid with laser radiation and chemical reaction through sinusoidal channels. *Waves in Random and Complex Media*, 1-22.
- [44]Eldesoky, I. M., Abdelsalam, S. I., El-Askary, W. A., & Ahmed, M. M. (2019). Concurrent development of thermal energy with magnetic field on a particle-fluid suspension through a porous conduit. *BioNanoScience*, 9(1), 186-202.

- [45] Shahid, A., Bhatti, M. M., Ellahi, R., & Mekheimer, K. S. (2022). Numerical experiment to examine activation energy and bi-convection Carreau nanofluid flow on an upper paraboloid porous surface: Application in solar energy. *Sustainable Energy Technologies and Assessments*, 52, 102029.
- [46] Trefethen, L. N. (2000). *Spectral methods in MATLAB*. Society for industrial and applied mathematics.
- [47] Sadeghy, K., Hajibeygi, H., & Taghavi, S. M. (2006). Stagnation-point flow of upper-convected Maxwell fluids. *International Journal of Non-Linear Mechanics*, 41(10), 1242-1247.
- [48] Subhas Abel, M., Tawade, J. V., & Nandeppanavar, M. M. (2012). MHD flow and heat transfer for the upper-convected Maxwell fluid over a stretching sheet. *Meccanica*, 47(2), 385-393.
- [49] Khan, W. A., & Pop, I. (2010). Boundary-layer flow of a nanofluid past a stretching sheet. *International Journal Heat and Mass Transfer*, 53(11-12), 2477-2483.
- [50] Ree, T., & Eyring, H. (1955). Theory of non-Newtonian flow. II. Solution system of high polymers. *Journal of Applied Physics*, 26(7), 800-809.